

# Mid-Infrared Thermal Radiation Harvesting using Uncooled Narrow Bandgap GeSn Thermophotovoltaic cell

G rard Daligou,<sup>†</sup> Mahmoud R. M. Atalla,<sup>†</sup> C dric Lemieux-Leduc,<sup>†</sup> Anthony  
Nomezine,<sup>†</sup> Simone Assali,<sup>†</sup> Richard Soref,<sup>‡</sup> and Oussama Moutanabbir<sup>\*,†</sup>

<sup>†</sup>*Department of Engineering Physics,  cole Polytechnique de Montr al, C.P. 6079, Succ.  
Centre-Ville, Montr al, Qu bec, Canada H3C 3A7*

<sup>‡</sup>*Department of Engineering, University of Massachusetts Boston, Boston, MA 02125, USA*

E-mail: oussama.moutanabbir@polymtl.ca

## Abstract

Thermophotovoltaic (TPV) cells are increasingly attractive for applications in industrial waste heat harvesting, aerospace energy management, and compact power generation. Deploying midwave-infrared (MWIR) TPV in practical applications requires narrow-bandgap semiconductors that not only absorb low-energy photons but also integrate with scalable, low-cost platforms. Although high-performance TPV devices have been demonstrated using III-V materials such as InAs, GaSb, and InGaAs(P), their use remains limited by cost and substrate size. With this perspective, narrow bandgap GeSn alloys are a promising alternative that extend group-IV absorption into the MWIR while being silicon-compatible. Although the potential of GeSn TPV cells has been predicted, no experimental demonstration has been reported. Here, proof-of-concept Ge<sub>0.91</sub>Sn<sub>0.09</sub>

*p-i-n* TPV diodes (1 mm diameter) grown on silicon were fabricated and their performance was benchmarked against commercial InAs and extended-InGaAs devices. Measurements at 300 K under 2.3  $\mu\text{m}$  laser and  $\sim 1500$  K SiC Global illumination revealed peak responsivity of  $\sim 0.2$  A/W and an output power of  $\sim 0.41$  mW/cm<sup>2</sup>. These devices show trends comparable to those of the InAs diode under identical conditions, although at reduced absolute levels. To assess the intrinsic performance potential, Poisson-drift-diffusion modeling incorporating experimentally calibrated emitter emissivity predicts power densities exceeding 1 W/cm<sup>2</sup> under moderate MWIR thermal illumination, indicating that the present devices operate far below their fundamental limits and are primarily constrained by defect-assisted recombination and transport losses. These results establish GeSn as a scalable, silicon-compatible MWIR TPV platform and highlight a larger performance potential achievable through material and device optimization.

## Introduction

The overlap of blackbody emission from sources in the 500-2000 K range with the mid-infrared portion of the electromagnetic spectrum has spurred strong interest in narrow bandgap thermophotovoltaic (TPV) technologies.<sup>1</sup> By directly converting thermal radiation into electricity, TPV devices are attractive for applications such as industrial waste heat harvesting, aerospace energy management, remote power generation, and portable devices.<sup>2-8</sup> In this spectral range, narrow bandgap semiconductors are required to achieve efficient photon absorption, raising additional challenges in materials development, radiation-matter interaction, carrier transport, and device fabrication.<sup>9</sup>

The development of TPV cells has historically mirrored advances in solar photovoltaic (PV), with early devices adapting conventional *p-n* junction architectures for infrared absorption.<sup>10,11</sup> Yet, the distinct requirements of MWIR TPV, including operation with lower-energy photons, management of thermalization losses, and the need for robust spectral control, have driven the exploration of specialized emitter, filter, and device architectures.<sup>8,12</sup>

In particular, transmissive spectral control using highly reflective back-surface mirrors has emerged as the most effective strategy to recycle sub-bandgap photons and enhance efficiency in far-field TPV operation.<sup>8,13</sup>

At the material level, most high-efficiency TPV devices demonstrated to date have relied on III-V compounds such as GaSb,<sup>14</sup> InGaAs(P),<sup>12,13,15</sup> and InAs,<sup>2,16</sup> owing to their favorable bandgaps and mature processing techniques. However, these materials face inherent limitations, including substrate high cost and small size, which restrict scalability for large-area deployment.<sup>17</sup> These challenges have motivated growing interest in group-IV alternatives, particularly germanium-tin (GeSn) alloys.<sup>9</sup> By tuning the Sn content and strain state, GeSn offers access to direct bandgaps in the MWIR while retaining compatibility with established silicon and germanium platforms.<sup>18</sup> This combination provides pathways toward cost-effective manufacturing, large wafer integration, and reduced material toxicity.

Recent progress in GeSn epitaxy and device processing has already enabled a variety of optoelectronic devices in the short- to the mid-wave infrared range,<sup>19–35</sup> underscoring the potential of the material for TPV applications. Several theoretical and numerical studies have predicted the performance of GeSn-based TPV devices, exploring bandgap tuning, layer thickness, and expected efficiencies under MWIR illumination.<sup>9,17,36–38</sup> However, to the best of our knowledge, no experimental demonstration of a GeSn TPV device has been reported. Building on this motivation, the present work reports a proof-of-concept GeSn TPV diode, demonstrating the feasibility of experimental radiation energy conversion in the MWIR and providing the basis for future performance optimization.

## Results and discussion

### Growth of GeSn epilayers

GeSn *p-i-n* heterostructures (HSs) were grown on 4-inch Si(100) substrates using reduced pressure chemical vapor deposition (RPCVD), following similar growth sequence and pa-

rameters to those used in Ref.<sup>39</sup> Substrate preparation involved HF-based surface cleaning, followed by the growth of Ge virtual substrate (VS). The latter is obtained through a three-step process: growth of an initial 600-700 nm-thick Ge layer, followed by thermal cycling annealing up to 800 °C, and a subsequent growth of an additional Ge layer to improve crystalline quality.<sup>40</sup> The active region comprises a GeSn-based vertical *p-i-n* junction formed atop a four-layer graded GeSn buffer. The *p*-type Ge<sub>0.94</sub>Sn<sub>0.06</sub>, intrinsic Ge<sub>0.91</sub>Sn<sub>0.09</sub>, and *n*-type Ge<sub>0.95</sub>Sn<sub>0.05</sub> layers were deposited at 335 °C, 305-315 °C, and 345 °C, respectively, using GeH<sub>4</sub> and SnCl<sub>4</sub> precursors. These growth temperatures were optimized to achieve the targeted Sn content and strain conditions required for a double HS with a direct bandgap *i*-layer, despite potential fluctuations in Sn incorporation caused by partial strain relaxation and/or the presence of dopants.<sup>20,39,41</sup> Doping was obtained using diborane (B<sub>2</sub>H<sub>6</sub>) and arsine (AsH<sub>3</sub>) precursors, yielding active carrier concentrations above 10<sup>19</sup> cm<sup>-3</sup>, as confirmed by capacitance-voltage measurements.<sup>39</sup> Two thin heavily doped *n*-type GeSn contact layers were deposited atop the *p-i-n* stack to reduce contact resistance and improve device performance. Note that the strain and microstructure of the as-grown double HS are identical to those reported in Ref.,<sup>39</sup> with layer thicknesses of 346 nm, 432 nm, and 242 nm, for the *p*-, *i*-, and *n*-layers, respectively. The Ge-VS exhibits an in-plane thermal mismatch-induced tensile strain of ~0.2%, while the GeSn buffer layers show relatively low compressive strain, reaching about -0.2% in the upper layers. Additionally, the *p*-layer is fully relaxed, the *i*-layer has a compressive strain of -0.24%, and the *n*-layer is slightly tensile strained, with a value of ~0.3%, as measured by X-ray diffraction reciprocal space mapping. Besides, transmission electron microscopy (not shown) indicates high crystalline quality in the *i*- and *n*-layers, while the *p*-layer and underlying buffer contain dislocations, particularly near the Si/Ge-VS interface.

## GeSn *p-i-n* devices

The GeSn photodiodes studied in this work were fabricated using a circular mesa vertical *p-i-n* architecture, with an active area diameter of up to 1 mm, as shown in Figure 1(a). While state-of-the-art TPV cells typically employ front metal gridlines combined with a full-area back contact to minimize series resistance,<sup>8,12,42</sup> the present design was intentionally chosen to minimize fabrication-related uncertainties and enables a focused assessment of the intrinsic junction behavior under TPV-relevant illumination conditions. The circular mesa geometry further provides a well-defined active area and uniform illumination, facilitating reproducible electrical and optical analyses. Although not optimized for maximum TPV efficiency, this architecture establishes a robust baseline for evaluating the potential of GeSn *p-i-n* devices for MWIR TPV applications. The process began with GeSn *p-i-n* surface cleaning using HF/HCl/H<sub>2</sub>O (1:1:2) solution. Photolithography was then performed to define the top mesa features, followed by anisotropic etching of the top *n*-type GeSn layer down to the *p*-type region using an inductively coupled plasma (ICP)-reactive ion etching (RIE) system with a Cl<sub>2</sub>/N<sub>2</sub>/O<sub>2</sub> chemistry. A second photolithography and etch step was carried out to further define an underlying mesa down to the Ge virtual substrate, effectively creating a double-mesa structure that enhances device isolation and reduces parasitic contact effects. After each dry etching step, sidewall passivation was performed using a brief immersion in HCl/HF (1:1) to remove surface oxides and suppress leakage paths. A  $\sim 1.5$   $\mu\text{m}$  thick SiO<sub>2</sub> passivation layer was then deposited by plasma-enhanced chemical vapor deposition (PECVD) to provide insulation and support low-capacitance contacts. Contact vias were patterned and opened through buffered oxide etching. Finally, metal contacts were formed by e-beam evaporation of a Ti/Au/Ag/Au multilayer stack, where Ag served to fill SiO<sub>2</sub> topography and minimize the total thickness of gold required for reliable contact pads.

Current-voltage (I-V) measurements were performed at 300 K using a source measure unit (SMU) connected to a probe station. The fabricated GeSn devices were evaluated under two illumination regimes: (i) laser-based power beaming and (ii) broadband TPV

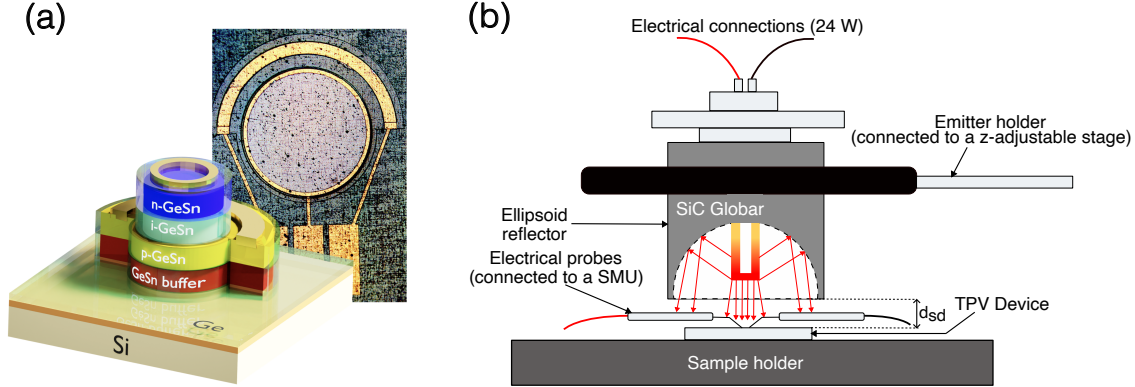


Figure 1:  $\text{Ge}_{0.94}\text{Sn}_{0.06}/\text{Ge}_{0.91}\text{Sn}_{0.09}/\text{Ge}_{0.95}\text{Sn}_{0.05}$  *p-i-n* device structure and SiC-based illumination setup. (a) Schematic and optical micrograph of a representative *p-i-n* TPV device. The glossy-like material covering the device represents the  $\text{SiO}_2$  passivation layer, whereas the gold-like structure on top on both the *p*- and *n*- GeSn layers are the metallic contacts. (b) Schematic of the measurement configuration for SiC-based TPV illumination, including beam delivery and device mounting stages.

operation. For power beaming, a  $2.3\ \mu\text{m}$  laser was directed onto the device after passing through optical components, including beam splitters, mirrors, and focusing lenses. For broadband operation, a SiC heating element served as the infrared emitter. This emitter is housed in an ellipsoid reflector to increase the optical output, and help in defining the beam size. The device was mounted on a sample holder equipped with *x-y* linear translation for alignment, while the emitter was positioned on a *z*-adjustable stage to vary the source-detector distance ( $d_{sd}$ ). This geometry enables tuning of the emitter-detector view factor (VF), defined as the overlap ratio between the source and detector active areas, which directly influences the optical coupling efficiency.<sup>43</sup> Figure 1(b) presents a schematic of the experimental setup. The SiC emitter, with a nominal color temperature of  $\sim 1500\ \text{K}$ , provides a gray-body spectrum extending from  $0.5$  to  $9.0\ \mu\text{m}$  based on the data provided by the supplier.<sup>44</sup> The spectrum of the SiC heating element was measured from  $0.4$  to  $5.6\ \mu\text{m}$ , as highlighted in Figure 2(a). The structures in the measured light source spectra are due to absorption from various molecules such as  $\text{H}_2\text{O}$  and  $\text{CO}_2$ .<sup>44</sup> Although manufacturer specifications do not include the spectral emissivity  $\varepsilon(\lambda)$ , this parameter is essential for accurate estimation of the emitted power. In practice,  $\varepsilon(\lambda)$  must be determined through

calibration against blackbody standards under comparable conditions.<sup>15</sup>

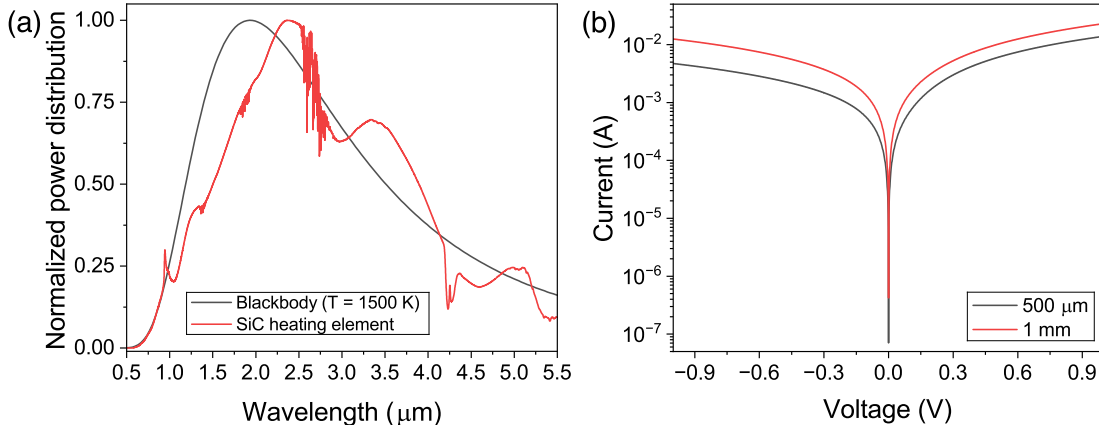


Figure 2: Broadband source characterization and dark I-V device characteristics. (a) Emission spectrum of the SiC heating element at  $\sim 1500$  K, highlighting its broadband gray-body distribution extending across the mid-infrared.<sup>44</sup> (b) I-V characteristics under dark condition for devices with  $500 \mu\text{m}$  and  $1 \text{ mm}$  active area diameter.

As a baseline, dark I-V characteristics were measured for GeSn devices with active areas of  $500 \mu\text{m}$  and  $1 \text{ mm}$ , as shown in Figure 2(b). Both devices exhibited relatively low rectification ratios across the applied bias range. Specifically, the  $500 \mu\text{m}$  device achieved a rectification ratio of approximately 2.48 at  $0.5 \text{ V}$ , whereas the  $1 \text{ mm}$  device reached only  $\sim 1.61$  at the same voltage. These observations reflect the impact of growth-related defects, which are more pronounced in larger-area devices. Reducing device dimensions is expected to enhance rectification significantly. For instance, prior work on similar GeSn structures demonstrated that decreasing the diameter from  $120 \mu\text{m}$  to  $28 \mu\text{m}$  can increase the rectification ratio by one to two orders of magnitude.<sup>20</sup> While smaller diameters (down to  $10 \mu\text{m}$ ) enable high-speed operation at room temperature (RT),<sup>45</sup> they are less favorable for power-generation applications, such as thermal radiation harvesting, where larger active areas are desirable. Thus, GeSn TPV devices require a careful balance between material quality, heterostructure design, and device size to optimize performance for their intended application.

With these configurations established, the GeSn diodes, with  $1 \text{ mm}$  active area diameter, were measured alongside state-of-the-art commercial InAs and extended-InGaAs photodiodes of identical geometry, enabling direct comparison of performance under identical condi-

tions. I-V characteristics were obtained in the dark, under  $2.3\ \mu\text{m}$  laser illumination ( $P_{in} = 5.14\ \text{mW}$ ), and under broadband infrared emission from a SiC Globar positioned  $\sim 3\ \text{cm}$  above the devices. Relative spectral responsivities ( $R_{sp}$ ) were measured, at  $0\ \text{V}$ , using a Fourier transform infrared (FTIR) spectrometer and calibrated against the InAs photovoltaic detector, which has a well-characterized response. The results, summarized in Figures 3 and 4, highlight key differences in current levels, responsivity, and overall performance. The GeSn device exhibits a peak responsivity of  $\sim 0.2\ \text{A/W}$  at  $\sim 1.7\ \mu\text{m}$ , remaining relatively constant up to  $2.1\ \mu\text{m}$  before gradually decreasing and cutting off near  $\sim 2.6\ \mu\text{m}$ . By comparison, the InAs detector peaks at  $\sim 1\ \text{A/W}$  at  $3.31\ \mu\text{m}$  with a cutoff around  $3.65\ \mu\text{m}$ , while the ext-InGaAs diode peaks at  $\sim 1.52\ \text{A/W}$  at  $2.31\ \mu\text{m}$  and cuts off near  $2.8\ \mu\text{m}$ . Under dark conditions (Figure 3(b)), the GeSn device shows a dark current levels similar to those of the InAs detector at  $0\ \text{V}$  ( $\sim 0.28\ \mu\text{A}$ ), although with a lower rectification ratio. Both devices exhibit dark currents approximately one order of magnitude higher than that of the ext-InGaAs detector, which records  $\sim 34.5\ \text{nA}$  at  $0\ \text{V}$  with a rectification ratio reaching  $\sim 4 \times 10^2$  at  $0.5\ \text{V}$ .

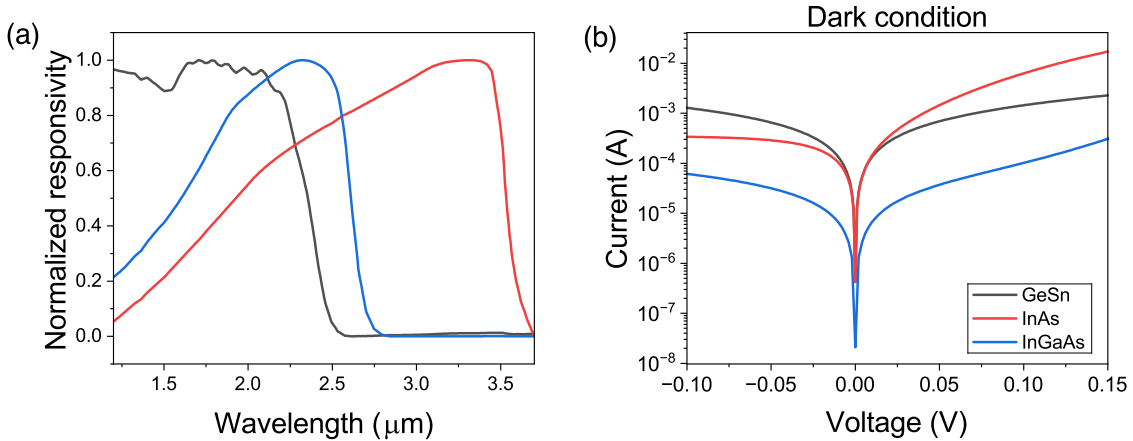


Figure 3: (a) Spectral responsivity at 300 K of GeSn, InAs, and extended-InGaAs photodiodes with identical active area diameters ( $1\ \text{mm}$ ), measured, at  $0\ \text{V}$ , using FTIR spectroscopy and calibrated against InAs. The responsivities were normalized to highlight the trends and the cutoff wavelengths. (b) Dark current-voltage (I-V) characteristics of the same devices at 300 K, showing comparable current levels for GeSn and InAs but lower rectification ratios compared to extended-InGaAs.

Under  $2.3\ \mu\text{m}$  laser illumination, all devices displayed clear photocurrent generation, confirming their photo-response. The GeSn device produced a short-circuit current ( $I_{sc}$ ) of approximately  $0.353\ \text{mA}$ , nearly three orders of magnitude higher than its dark current at  $0\ \text{V}$ , with an open-circuit voltage ( $V_{oc}$ ) of  $\sim 24\ \text{mV}$ , corresponding to an output power density of  $0.27\ \text{mW}/\text{cm}^2$ . The InAs detector showed higher  $I_{sc}$  and  $V_{oc}$  under identical conditions, resulting in an output power density of  $\sim 7.9\ \text{mW}/\text{cm}^2$ , while the ext-InGaAs detector delivered the highest output with  $I_{sc} \approx 3.97\ \text{mA}$ ,  $V_{oc} \approx 0.21\ \text{V}$ , and a peak electrical output power density of  $37\ \text{mW}/\text{cm}^2$ . These differences are consistent with the higher responsivity of ext-InGaAs at the excitation wavelength. When illuminated with the broadband SiC emitter (Figure 1(b)), all devices showed enhanced photocurrents compared to dark conditions, following the same relative performance trends as under laser excitation. The GeSn detector achieved an output power density of  $\sim 0.41\ \text{mW}/\text{cm}^2$ , while the InAs and ext-InGaAs detectors reached  $\sim 4.3\ \text{mW}/\text{cm}^2$  and  $\sim 64\ \text{mW}/\text{cm}^2$ , respectively. The observed differences in current levels and slope between laser and SiC illumination can be attributed to the distinct spectral distribution and optical flux of the two sources.

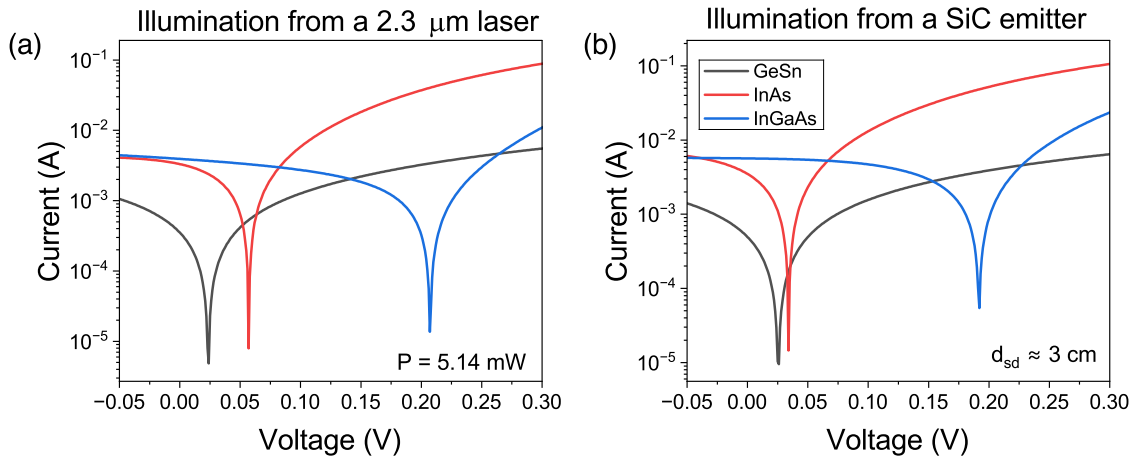


Figure 4: (a) I-V response of GeSn, InAs, and extended-InGaAs photodiodes under  $2.3\ \mu\text{m}$  laser illumination, demonstrating photoresponse and output power density differences among the devices. (b) I-V characteristics under broadband mid-infrared radiation from a  $\sim 1500\ \text{K}$  SiC emitter positioned  $3\ \text{cm}$  above the detectors, reproducing trends observed under laser illumination.

The observed performance differences among the three devices can be primarily attributed

to material maturity, processing optimization, and inherent device properties. The GeSn diode, as a first proof-of-concept MWIR TPV device, exhibits measurable photocurrent and energy conversion, although dark currents and voltage output remain below those of the commercial InAs and ext-InGaAs detectors. The InAs device benefits from established growth and fabrication techniques, yielding improved photoresponse, while the ext-InGaAs detector achieves the highest performance under both illumination conditions, consistent with its optimized material quality and responsivity at the wavelengths tested.

To further quantify the intrinsic performance potential of GeSn-based TPV devices and to contextualize the experimental results, numerical modeling was employed. While experimental measurements provide direct insight into device operation under thermal illumination, they do not isolate the relative contributions of material quality, recombination mechanisms, and carrier transport limitations. Device-level simulations can provide a complementary framework to establish realistic efficiency benchmarks and to evaluate the achievable power conversion efficiency of GeSn TPV cells under mid-infrared thermal radiation. The modeling approach adopted in this work is based on a one-dimensional coupled Poisson-drift-diffusion framework previously developed for TPV devices.<sup>9</sup> The simulated *p-i-n* GeSn structure corresponds directly to the fabricated device, with layer thicknesses, doping concentrations, and material parameters selected to match the measured devices. The optical generation rate within the multilayer GeSn stack is calculated using the optical transfer matrix method, while the electrical model explicitly accounts for intrinsic and extrinsic recombination mechanisms relevant to narrow-bandgap group-IV semiconductors. Note that parasitic resistances are neglected and ideal ohmic contacts are assumed; therefore, the simulated performance represents an upper bound for the fabricated devices. The spectral emissivity of the SiC thermal emitter was taken from the work of Fan et al.,<sup>15</sup> where the same lamp geometry and operating conditions were used and the emissivity was experimentally calibrated. Using these emissivity data, the incident photon flux and power density on the TPV device were calculated and used as input to the model. For the experimental configuration, the incident

power density was estimated to be approximately  $16 \text{ W/cm}^2$ .

Using mobility, surface recombination rates, Auger coefficients, and the SRH capture lifetimes extracted from Ge as a practical baseline, due to the lack of detailed experimental parameters of GeSn materials,<sup>46–49</sup> the modeled GeSn device exhibits a short-circuit current of approximately 34 mA and an open-circuit voltage of approximately 0.41 V, corresponding to a peak electrical output power density of  $\sim 1.37 \text{ W/cm}^2$ . Despite the moderate incident power density, the simulated device performance significantly exceeds the experimentally measured values, with  $I_{sc}$ ,  $V_{oc}$ , and  $P_{max}$  being higher by factors of approximately 69, 16, and 3000, respectively. This large difference indicates that the fabricated GeSn TPV devices operate far from their intrinsic performance limits and that non-ideal material and transport effects dominate the measured response. In particular, the simulations neglect parasitic resistances, non-uniform illumination, and contact losses, all of which are expected to reduce carrier collection and photovoltage in practical devices. More importantly, the deviation between modeled and measured characteristics points toward strong non-radiative recombination losses in the GeSn absorber. At the injection and doping levels relevant to the present TPV conditions, Auger recombination is not expected to be the dominant loss mechanism. Instead, Shockley-Read-Hall (SRH) recombination is expected to play a central role in governing carrier lifetime, collection efficiency, and photovoltage. In GeSn alloys, SRH recombination is further exacerbated by the presence of misfit dislocations, point defects, and interface states associated with strain relaxation and heteroepitaxial growth on Ge/Si substrates.<sup>18,50</sup>

To illustrate the impact of defect-assisted recombination on GeSn TPV performance, simulations were performed for different SRH capture lifetimes  $\tau_{n0}$ ,  $\tau_{p0}$ . Because carrier-specific SRH parameters in GeSn are not well established, equal electron and hole capture lifetimes ( $\tau_{n0} = \tau_{p0} = \tau_0$ ) are assumed, with  $\tau_0$  treated as an effective bulk lifetime reflecting the defect density. In addition to the Ge-like baseline ( $\tau_0 = 2 \times 10^{-6} \text{ s}$ ) mentioned above, two additional  $\tau_0$  values have been chosen to represent moderate defect density ( $\tau_0 = 1 \times 10^{-8} \text{ s}$ )

and defect-dominated regime ( $\tau_0 \sim 1 \times 10^{-10}$  s). These values span the range expected for heteroepitaxial GeSn alloys and enable the estimation of the progressive degradation of  $V_{oc}$ ,  $I_{sc}$ , and output power density with increasing non-radiative recombination.<sup>18,51</sup> Reducing  $\tau_0$  to  $1 \times 10^{-8}$  s leads to a decrease in  $V_{oc}$  to 0.28 V and a corresponding reduction in peak power density to  $\sim 0.71$  W/cm<sup>2</sup>, while  $I_{sc}$  decreases more moderately to 29.4 mA. In the defect-dominated regime,  $V_{oc}$  collapses to  $\sim 0.09$  V and  $P_{max}$  is reduced by approximately 1.5 orders of magnitude compared to the Ge-like case, and  $I_{sc}$  reached a value of 10.14 mA. These results highlight the dominant role of SRH recombination in limiting the voltage and power output of present GeSn TPV devices.

Finally, it is also important to mention that one of the primary limitations that need to be addressed in TPV studies is rooted in the difficulty to accurately estimate the power emitted by the SiC source and, consequently, the power conversion efficiency (PCE) of the devices. The lack of a standardized method for estimating PCE makes comparisons across studies challenging and slows the systematic development of TPV devices.<sup>12,13,52</sup> Two main strategies have been broadly adopted for estimating absorbed power in TPV systems.<sup>52-54</sup> The first relies on optical characterization, measuring the spectral emissivity of the emitter and the reflectance of the cell to estimate net absorbed radiation.<sup>53</sup> This approach requires careful consideration of geometric effects, such as the emitter-cell view factor, and the angle- and temperature-dependent optical properties of both surfaces.<sup>53,54</sup> While relatively straightforward, this approach is highly sensitive to uncertainties in reflectance and assumes idealized radiative exchange conditions, limiting its accuracy for realistic device configurations.<sup>13,54</sup> The second approach relies on calorimetry, quantifying absorbed energy by measuring heat flow through the device.<sup>7,10,13,52</sup> The principle is that all the absorbed incident energy is either dissipated as heat or converted to electrical power. This method is best suited for systems with a high emitter-cell view factor, where thermal losses can be monitored directly, but its practical implementation is challenging due to thermal management requirements and geometric constraints.<sup>52</sup> Both approaches highlight the importance of careful emitter-device

alignment, thermal control, and accurate characterization of optical and thermal properties.

## Conclusion

In this work, proof-of-concept GeSn-based TPV diode is demonstrated, establishing GeSn as a viable silicon-compatible platform for MWIR energy conversion. A 1 mm-diameter vertical GeSn *p-i-n* device grown on silicon was fabricated and benchmarked against commercial InAs and extended-InGaAs detectors under both monochromatic (2.3  $\mu\text{m}$ ) and broadband thermal ( $\sim 1500\text{ K SiC}$ ) illumination. The measured peak responsivity and output power densities are  $\sim 0.2\text{ A/W}$  and  $\sim 0.41\text{ W/cm}^2$ , respectively. GeSn devices were found to exhibit trends comparable to commercial InAs device under identical experimental conditions, although at reduced absolute levels. GeSn TPV performance is limited primarily by defect-assisted recombination, non-ideal transport, elevated dark currents, and contact effects, highlighting the need for continued advances in epitaxial growth, heterostructure design, and contact engineering. To quantify the intrinsic performance potential, device-level Poisson-drift-diffusion simulations were performed. The modeling predicts power densities exceeding  $1\text{ W/cm}^2$  under moderate exposure to mid-infrared thermal radiation, indicating that the current GeSn devices operate far from their optimal performance and that substantial gains are achievable through lifetime and defect-density improvements. At the system level, emitter-detector coupling and standardized efficiency measurements remain essential to enable reliable benchmarking across TPV platforms. Overall, these results provide the experimental validation of GeSn TPV devices and reveal a large untapped performance margin. With continued progress in material quality, device architecture, and system integration, GeSn is poised to complement III-V TPV technologies and enable scalable, silicon-compatible MWIR energy harvesting platforms.

## Acknowledgement

The authors acknowledge support from NSERC Canada, Canada Research Chairs, Canada Foundation for Innovation, PRIMA Québec, Defence Canada (Innovation for Defence Excellence and Security, IDEaS), the European Union’s Horizon Europe research and innovation program under Grant Agreement No 101070700 (MIRAQLS), and the Air Force Office of Scientific and Research Grant No. FA9550-23-1-0763.

## References

- (1) Meyer, J. R. et al. Midinfrared Semiconductor Photonics - A Roadmap. 2025; <https://arxiv.org/abs/2511.03868>.
- (2) Lu, Q.; Zhou, X.; Krysa, A.; Marshall, A.; Carrington, P.; Tan, C.-H.; Krier, A. InAs Thermophotovoltaic Cells with High Quantum Efficiency for Waste Heat Recovery Applications below 1000°C. *Solar Energy Materials and Solar Cells* **2018**, *179*, 334–338.
- (3) Chan, W. R.; Stelmakh, V.; Karnani, S.; Waits, C. M.; Soljacic, M.; Joannopoulos, J. D.; Celanovic, I. Towards a Portable Mesoscale Thermophotovoltaic Generator. *Journal of Physics: Conference Series* **2018**, *1052*, 012041.
- (4) Wang, X.; Liang, R.; Fisher, P.; Chan, W.; Xu, J. Radioisotope Thermophotovoltaic Generator Design Methods and Performance Estimates for Space Missions. *Journal of Propulsion and Power* **2020**, *36*, 593–603.
- (5) Rizzo, L.; Federici, J. F.; Gatley, S.; Gatley, I.; Zunino, J. L.; Duncan, K. J. Comparison of Terahertz, Microwave, and Laser Power Beaming Under Clear and Adverse Weather Conditions. *Journal of Infrared, Millimeter, and Terahertz Waves* **2020**, *41*, 979–996.
- (6) Yang, R. Q.; Huang, W.; Santos, M. B. Narrow Bandgap Photovoltaic Cells. *Solar Energy Materials and Solar Cells* **2022**, *238*, 111636.

- (7) LaPotin, A.; Schulte, K. L.; Steiner, M. A.; Buznitsky, K.; Kelsall, C. C.; Friedman, D. J.; Tervo, E. J.; France, R. M.; Young, M. R.; Rohskopf, A.; Verma, S.; Wang, E. N.; Henry, A. Thermophotovoltaic Efficiency of 40%. *Nature* **2022**, *604*, 287–291.
- (8) Chen, S.; Guo, Y.; Pan, Q.; Shuai, Y. A Review on Current Development of Thermophotovoltaic Technology in Heat Recovery. *International Journal of Extreme Manufacturing* **2024**, *6*, 022009.
- (9) Daligou, G.; Soref, R.; Attiaoui, A.; Hossain, J.; Atalla, M. R.; Del Vecchio, P.; Moutanabbir, O. Group IV Mid-Infrared Thermophotovoltaic Cells on Silicon. *IEEE Journal of Photovoltaics* **2023**, *13*, 728–735.
- (10) Swanson, R. Silicon Photovoltaic Cells in Thermophotovoltaic Energy Conversion. 1978 International Electron Devices Meeting. 1978; pp 70–73.
- (11) Wedlock, B. Thermo-Photo-Voltaic Energy Conversion. *Proceedings of the IEEE* **1963**, *51*, 694–698.
- (12) Roy-Layinde, B.; Lim, J.; Arneson, C.; Forrest, S. R.; Lenert, A. High-Efficiency Air-Bridge Thermophotovoltaic Cells. *Joule* **2024**, *8*, 2135–2145.
- (13) Tervo, E. J. et al. Efficient and Scalable GaInAs Thermophotovoltaic Devices. *Joule* **2022**, *6*, 2566–2584.
- (14) Fraas, L.; Samaras, J.; Huang, H.; Minkin, L.; Avery, J.; Daniels, W.; Hui, S. TPV generators using the radiant tube burner configuration. Proceedings of 17th European PV Solar Energy Conference, Munich, Germany. 2001.
- (15) Fan, D.; Burger, T.; McSherry, S.; Lee, B.; Lenert, A.; Forrest, S. R. Near-Perfect Photon Utilization in an Air-Bridge Thermophotovoltaic Cell. *Nature* **2020**, *586*, 237–241.

- (16) Selvidge, J.; France, R. M.; Goldsmith, J.; Solanki, P.; Steiner, M. A.; Tervo, E. J. Large Area Near-Field Thermophotovoltaics for Low Temperature Applications. *Advanced Materials* **2025**, *37*, 2411524.
- (17) Lemire, A.; Grossklaus, K. A.; Vandervelde, T. E. Germanium-Tin Diode for Thermophotovoltaic Energy Collection. 2023 IEEE 50th Photovoltaic Specialists Conference (PVSC). 2023; pp 1–3.
- (18) Moutanabbir, O.; Assali, S.; Gong, X.; O'Reilly, E.; Broderick, C. A.; Marzban, B.; Witzens, J.; Du, W.; Yu, S.-Q.; Chelnokov, A.; Buca, D.; Nam, D. Monolithic Infrared Silicon Photonics: The Rise of (Si)GeSn Semiconductors. *Applied Physics Letters* **2021**, *118*, 110502.
- (19) Atalla, M. R. M.; Assali, S.; Attiaoui, A.; Lemieux-Leduc, C.; Kumar, A.; Abdi, S.; Moutanabbir, O. All-Group IV Transferable Membrane Mid-Infrared Photodetectors. *Advanced Functional Materials* **2021**, *31*, 2006329.
- (20) Atalla, M. R. M.; Assali, S.; Koelling, S.; Attiaoui, A.; Moutanabbir, O. High-Bandwidth Extended-SWIR GeSn Photodetectors on Silicon Achieving Ultrafast Broadband Spectroscopic Response. *ACS Photonics* **2022**, *9*, 1425–1433.
- (21) Buca, D.; Bjelajac, A.; Spirito, D.; Concepción, O.; Gromovyi, M.; Sakat, E.; Lafosse, X.; Ferlazzo, L.; von den Driesch, N.; Ikonic, Z.; Grützmacher, D.; Capellini, G.; El Kurdi, M. Room Temperature Lasing in GeSn Microdisks Enabled by Strain Engineering. *Advanced Optical Materials* **2022**, *10*, 2201024.
- (22) Chang, C.-Y.; Yeh, P.-L.; Jheng, Y.-T.; Hsu, L.-Y.; Lee, K.-C.; Li, H.; Cheng, H. H.; Chang, G.-E. Mid-Infrared Resonant Light Emission from GeSn Resonant-Cavity Surface-Emitting LEDs with a Lateral p-i-n Structure. *Photonics Research* **2022**, *10*, 2278–2286.

- (23) Chrétien, J. et al. GeSn Lasers Covering a Wide Wavelength Range Thanks to Uniaxial Tensile Strain. *ACS Photonics* **2019**, *6*, 2462–2469.
- (24) Chrétien, J.; Thai, Q. M.; Frauenrath, M.; Casiez, L.; Chelnokov, A.; Reboud, V.; Hartmann, J. M.; El Kurdi, M.; Pauc, N.; Calvo, V. Room Temperature Optically Pumped GeSn Microdisk Lasers. *Applied Physics Letters* **2022**, *120*, 051107.
- (25) Elbaz, A. et al. Ultra-Low-Threshold Continuous-Wave and Pulsed Lasing in Tensile-Strained GeSn Alloys. *Nature Photonics* **2020**, *14*, 375–382.
- (26) Joo, H.-J.; Kim, Y.; Burt, D.; Jung, Y.; Zhang, L.; Chen, M.; Parluhutan, S. J.; Kang, D.-H.; Lee, C.; Assali, S.; Ikonic, Z.; Moutanabbir, O.; Cho, Y.-H.; Tan, C. S.; Nam, D. 1D Photonic Crystal Direct Bandgap GeSn-on-insulator Laser. *Applied Physics Letters* **2021**, *119*, 201101.
- (27) Jung, Y.; Burt, D.; Zhang, L.; Kim, Y.; Joo, H.-J.; Chen, M.; Assali, S.; Moutanabbir, O.; Tan, C. S.; Nam, D. Optically Pumped Low-Threshold Microdisk Lasers on a GeSn-on-insulator Substrate with Reduced Defect Density. *Photonics Research* **2022**, *10*, 1332–1337.
- (28) Li, X.; Peng, L.; Liu, Z.; Zhou, Z.; Zheng, J.; Xue, C.; Zuo, Y.; Chen, B.; Cheng, B. 30 GHz GeSn Photodetector on SOI Substrate for 2  $\mu\text{m}$  Wavelength Application. *Photonics Research* **2021**, *9*, 494–500.
- (29) Liu, X.; Zheng, J.; Niu, C.; Liu, T.; Huang, Q.; Li, M.; Zhang, D.; Pang, Y.; Liu, Z.; Zuo, Y.; Cheng, B. Sn Content Gradient GeSn with Strain Controlled for High Performance GeSn Mid-Infrared Photodetectors. *Photonics Research* **2022**, *10*, 1567–1574.
- (30) Luo, L.; Assali, S.; Atalla, M. R. M.; Koelling, S.; Attiaoui, A.; Daligou, G.; Martí, S.; Arbiol, J.; Moutanabbir, O. Extended-SWIR Photodetection in All-Group IV Core/Shell Nanowires. *ACS Photonics* **2022**, *9*, 914–921.

- (31) Marzban, B.; Seidel, L.; Liu, T.; Wu, K.; Kiyek, V.; Zoellner, M. H.; Ikonc, Z.; Schulze, J.; Grützmacher, D.; Capellini, G.; Oehme, M.; Witzens, J.; Buca, D. Strain Engineered Electrically Pumped SiGeSn Microring Lasers on Si. *ACS Photonics* **2022**, 217–224.
- (32) Talamas Simola, E.; Kiyek, V.; Ballabio, A.; Schlykow, V.; Frigerio, J.; Zucchetti, C.; De Iacovo, A.; Colace, L.; Yamamoto, Y.; Capellini, G.; Grützmacher, D.; Buca, D.; Isella, G. CMOS-Compatible Bias-Tunable Dual-Band Detector Based on GeSn/Ge/Si Coupled Photodiodes. *ACS Photonics* **2021**, 8, 2166–2173.
- (33) Tran, H. et al. Si-Based GeSn Photodetectors toward Mid-Infrared Imaging Applications. *ACS Photonics* **2019**, 6, 2807–2815.
- (34) Xu, S.; Wang, W.; Huang, Y.-C.; Dong, Y.; Masudy-Panah, S.; Wang, H.; Gong, X.; Yeo, Y.-C. High-Speed Photo Detection at Two-Micron-Wavelength: Technology Enablement by GeSn/Ge Multiple-Quantum-Well Photodiode on 300 Mm Si Substrate. *Optics Express* **2019**, 27, 5798.
- (35) Zhou, Y. et al. Electrically Injected GeSn Lasers on Si Operating up to 100 K. *Optica* **2020**, 7, 924–928.
- (36) Conley, B. R.; Naseem, H.; Sun, G.; Sharps, P.; Yu, S.-Q. High efficiency MJ solar cells and TPV using SiGeSn materials. 2012 38th IEEE Photovoltaic Specialists Conference. 2012; pp 001189–001192.
- (37) Zhu, X.-M.; Cui, M.; Wang, Y.; Yu, T.-J.; Deng, J.-X.; Gao, H.-L. GeSn (0.524 eV) Single-Junction Thermophotovoltaic Cells Based on the Device Transport Model. *Chinese Physics B* **2022**, 31, 058801.
- (38) Tang, Y.; Liu, Y.; Yuan, C.; Tang, L.; Shao, J. Comparison of Optimized GeSn/Si Heterojunction and GaInAsSb/GaSb Thermophotovoltaic Cells with Similar Bandgaps. *Physica Scripta* **2023**, 98, 115516.

- (39) Atalla, M. R. M.; Assali, S.; Daligou, G.; Attiaoui, A.; Koelling, S.; Daoust, P.; Moutanabbir, O. Continuous-Wave GeSn Light-Emitting Diodes on Silicon with 2.5  $\mu\text{m}$  Room-Temperature Emission. *ACS Photonics* **2024**, *11*, 1335–1341.
- (40) Assali, S.; Nicolas, J.; Mukherjee, S.; Dijkstra, A.; Moutanabbir, O. Atomically Uniform Sn-rich GeSn Semiconductors with 3.0–3.5  $\mu\text{m}$  Room-Temperature Optical Emission. *Applied Physics Letters* **2018**, *112*, 251903.
- (41) Assali, S.; Nicolas, J.; Moutanabbir, O. Enhanced Sn Incorporation in GeSn Epitaxial Semiconductors via Strain Relaxation. *Journal of Applied Physics* **2019**, *125*, 025304.
- (42) Burger, T.; Sempere, C.; Roy-Layinde, B.; Lenert, A. Present Efficiencies and Future Opportunities in Thermophotovoltaics. *Joule* **2020**, *4*, 1660–1680.
- (43) Lim, J.; Forrest, S. R. Limits to the Energy-Conversion Efficiency of Air-Bridge Thermophotovoltaics. *Physical Review Applied* **2023**, *19*, 034099.
- (44) Global light source. [https://www.thorlabs.com/\\_sd.cfm?fileName=CTN002679-D02.pdf&partNumber=SLS203L](https://www.thorlabs.com/_sd.cfm?fileName=CTN002679-D02.pdf&partNumber=SLS203L), [Online] Accessed: 2025-08-11.
- (45) Atalla, M. R. M.; Lemieux-Leduc, C.; Assali, S.; Koelling, S.; Daoust, P.; Moutanabbir, O. Extended short-wave infrared high-speed all-GeSn PIN photodetectors on silicon. *APL Photonics* **2024**, *9*.
- (46) Caughey, D.; Thomas, R. Carrier Mobilities in Silicon Empirically Related to Doping and Field. *Proceedings of the IEEE* **1967**, *55*, 2192–2193.
- (47) Liu, J.; Sun, X.; Pan, D.; Wang, X.; Kimerling, L. C.; Koch, T. L.; Michel, J. Tensile-strained, n-type Ge as a gain medium for monolithic laser integration on Si. *Opt. Express* **2007**, *15*, 11272–11277.

- (48) Virgilio, M.; Manganelli, C. L.; Grosso, G.; Schroeder, T.; Capellini, G. Photoluminescence, Recombination Rate, and Gain Spectra in Optically Excited  $n$ -Type and Tensile Strained Germanium Layers. *Journal of Applied Physics* **2013**, *114*, 243102.
- (49) Bosi, M.; Attolini, G. Germanium: Epitaxy and Its Applications. *Progress in Crystal Growth and Characterization of Materials* **2010**, *56*, 146–174.
- (50) Giunto, A.; Fontcuberta i Morral, A. Defects in Ge and GeSn and their impact on optoelectronic properties. *Applied Physics Reviews* **2024**, *11*, 041333.
- (51) Julsgaard, B.; von den Driesch, N.; Tidemand-Lichtenberg, P.; Pedersen, C.; Ikonic, Z.; Buca, D. Carrier lifetime of GeSn measured by spectrally resolved picosecond photoluminescence spectroscopy. *Photon. Res.* **2020**, *8*, 788–798.
- (52) López, E.; Artacho, I.; Datas, A. Thermophotovoltaic Conversion Efficiency Measurement at High View Factors. *Solar Energy Materials and Solar Cells* **2023**, *250*, 112069.
- (53) Mahorter, R. G.; Wernsman, B.; Thomas, R. M.; Siergiejs, R. R. Thermophotovoltaic System Testing. *Semiconductor Science and Technology* **2003**, *18*, S232–S238.
- (54) Narayan, T. C. et al. Platform for Accurate Efficiency Quantification of  $> 35\%$  Efficient Thermophotovoltaic Cells. 2021 IEEE 48th Photovoltaic Specialists Conference (PVSC). 2021; pp 1352–1354.